5-1-2016

Neutron-Gamma Discrimination in Elpasolite Scintillator Detector

Brittany Morgan
University of Nevada, Las Vegas, morga214@unlv.nevada.edu

NEUTRON-GAMMA DISCRIMINATION IN ELPASOLITE SCINTILLATOR DETECTOR

By

Brittany Morgan

Bachelor of Arts - Physics
Seattle University
2011

A thesis submitted in partial fulfillment
of the requirements for the
Master of Science - Materials and Nuclear Engineering

Department of Mechanical Engineering
Howard R. Hughes College of Engineering
The Graduate College

University of Nevada, Las Vegas
May 2016

UNLV | GRADUATE COLLEGE

Thesis Approval

The Graduate College
The University of Nevada, Las Vegas

April 15, 2016

This thesis prepared by

Brittany Morgan

entitled

Neutron-Gamma Discrimination in Elpasolite Scintillator Detector

is approved in partial fulfillment of the requirements for the degree of

Master of Science - Materials and Nuclear Engineering
Department of Mechanical Engineering

Alexander Barzilov, Ph.D.
Examination Committee Chair

Kathryn Hausbeck Korgan, Ph.D.
Graduate College Interim Dean

William Culbreth, Ph.D.
Examination Committee Member

Yi-Tung Chen, Ph.D.
Examination Committee Member

Gary Cerefice, Ph.D.
Graduate College Faculty Representative

ABSTRACT

Neutron-Gamma Discrimination in Elpasolite Scintillator Detector

by

Brittany Morgan

Dr. Alexander Barzilov, Examination Committee Chair

Associate Professor of Mechanical Engineering

University of Nevada, Las Vegas

Existing nuclear stockpiles and weapons-making capabilities imperil the global community. Current nonproliferation efforts involve the research and development of newer, more efficient detection systems that can be deployed for the interdiction and monitoring of special nuclear materials (SNM). Spontaneous and induced fission events in SNM produce neutrons and gamma rays, which can be detected and analyzed, in particular, using scintillator detectors. Various electronic data acquisition systems and data analysis methods have been employed to record and characterize neutron and photon signatures. The goal of this thesis is to develop a new method of discrimination between photons and neutrons in the CLYC elpasolite scintillator detector.

Because neutrons and photons interact uniquely with scintillator materials, they generate scintillation light decay signals of different time profiles. Several conventional and digital pulse shape discrimination (PSD) methods exist to exploit the different features of detector signal waveforms caused by the different time profiles of the scintillation decay. They can be categorized on the basis of their implementation: time domain only or time and frequency domain. In this study, wavelet analysis is implemented in the time domain. When the discrete wavelet transform

is applied to each pulse, the Haar wavelet is sampled over the signal to generate a set of coefficients, which are then further analyzed using numerical integration. The wavelet-based signal analysis code has been written in Matlab. The code processes a single detector waveform at a time. It first applies the discrete wavelet transform to smooth the waveform, and then calculates the power of this signal. After performing partial integrations on different parts of the coefficients' curve, it calculates the radiation identification (RID) value that serves as a threshold for neutron-gamma discrimination. Beyond the identifying threshold, the signal is categorized as a neutron event; below it is categorized as a photon event.

Plots of the total integral under the power of the waveform versus RID values and counts versus RID values were generated to visualize the PSD properties; the figure of merit (FOM) of the PSD method was calculated. The FOM quantifies the quality of neutron-gamma discrimination. The PSD algorithm and the Matlab code were developed and tested on the set of neutron and photon waveforms experimentally measured with the CLYC detector and excellent neutron-gamma separation was observed.

ACKNOWLEDGEMENTS

First, I would like to thank my advisor and committee members for pushing me through this endeavor: Dr. Barzilov, Dr. Cerefice, Dr. Culbreth, and Dr. Chen.

Dr. Barzilov, thank you for the invaluable support and guidance. I needed the push and direction to pursue this project.

Dr. Cerefice, thank you for the countless office hours for coursework help and academic advice. Your open-door policy has been a great source of solace for me and many other students.

Dr. Culbreth, thank you for integrating coursework with your humor-enriched life experience. It has been a wonderful supplement to my education.

Dr. Chen, thank you for introducing me to the Mechanical Engineering Department at UNLV. You were Graduate Coordinator when I was applying, and if I hadn't met with you, I wouldn't have chosen to pursue nuclear engineering.

A special thanks to Joan Conway and Jim Boyer: thank you so much for keeping me organized and handling all of my logistical needs. You two are amazing – I really appreciate your help!

I would also like to thank my friends from the Mechanical Engineering Department at UNLV: Matt Hodges, Jessica Hartman, David Chu, and Amber Guckes. Thank you for all the help and support. I could not have completed this work without all of you.

Lastly, I would like to recognize my coworkers and supervisors at NSTec: Irene Garza, Pat O'Gara, Rob Buckles, and Dr. Aaron Luttman. Your support and flexibility were crucial to my success.

TABLE OF CONTENTS

LIST OF TABLES

LIST OF FIGURES

CHAPTER 1 - INTRODUCTION

1.1 Background

Growth of the nuclear industry has introduced a number of avenues that utilize radiation detection technologies. Some examples of applications that would benefit from the capability to discriminate between radiation types include, but are not limited to, the following [1]:

1. Nuclear medicine and radiation oncology involve extensive use of radiological imaging and therapy techniques which are implemented using radiation detectors [2];
2. Interdisciplinary research projects conducted at national laboratories such as DOE's spallation neutron source necessitate accurate, efficient neutron detectors [3];
3. Industrial plants monitor corrosion with neutron radiography [4]; the strong attenuation of neutrons causes high sensitivity in metals yielding a detailed radiograph of industrial materials;
4. Inertial and magnetic confinement fusion research [5] requires neutron detection to determine the presence or absence of fusion in experimentation; and, lastly,
5. Nuclear power plants mandate facility and personnel monitoring for general health and safety of workers and the environment [6].

Current political climate, however, has warranted nonproliferation, safeguards and security as the primary motivations for advancement of radiation detection technologies. Despite the end of the Cold War over two decades ago, nuclear weapons stockpiles continue to imperil the international community. Russia and the United States respectively possess approximately 7500 and 7200 nuclear weapons, accounting for over 90% of the global stockpile [7], while other countries account for the remaining 10%.

Ready-made weapons of mass destruction are not, however, the sole nuclear threat to global security. Mere weapons-making capability and retention of special nuclear materials likewise plague the international community, as demonstrated recently in the nuclear deal between the United States and Iran [8], which involved the dismantling of centrifuges and surrender of fuel – in summary, a renouncement of a potential nuclear weapons program. The reality is that with world-wide development of new nuclear technologies, there will be continued need for nuclear nonproliferation efforts.

In addition to proliferation issues, other threats such as cyber-attacks pose danger to the nuclear industry, according to the Nuclear Threat Initiative Security Index [9], the most recent documented event being the Stuxnet virus [10]. While tackling cyber security is its own issue, considerable physical measures must be taken to secure special nuclear materials. SNM is defined by the Atomic Energy Act of 1954 as plutonium, uranium-233, uranium enriched in either uranium-233 or uranium-235, and other material as determined by the Nuclear Regulatory Commission (NRC) [11]. It is categorized "according to the risk and potential for its direct use in a clandestine fissile explosive or for its use in the production of nuclear material for use in a fissile explosive" [12]. The NRC Safeguard categories of SNM [12] are listed in Table 1.

Table 1: Safeguard Categories of SNM

Category	Nuclide	Minimum Quantity (grams or kilograms)
I: Strategic SNM	U-235 contained in HEU*	≥ 5 kg
	U-233	≥ 2 kg
	Pu	≥ 2 kg
	Any combination of U-235 in HEU, U-233, and Pu*	≥ 5 kg
II: Special Nuclear Material of Moderate Strategic Significance	U-235 contained in HEU*	> 1 kg, but < 5 kg
	U-235 contained in LEU**	≥ 10 kg
	U-233	≥ 500 g, but < 2 kg
	Pu	≥ 500 g, but < 2 kg
	Combined quantity = (g U-235) + 2(g U-233 + g Pu)	> 1000 g, but < 2 kg
III: Special Nuclear Material of Low Strategic Significance	U-235 contained in HEU*	> 15 g, but < 1 kg
	U-235 contained in LEU**	> 1 kg, but < 10 kg
	U-233	> 15 g, but < 500 g
	Pu	>15 g, but < 500 g
	Combined quantity = (g U-235) + (g U-233) + (g Pu)	>15 g
* *Highly Enriched Uranium: ≥ 20% enriched in U-235* ** *Low-Enriched Uranium: < 20% enriched in U-235*		

Category I SNM, as shown in Table 1, clearly poses the most consequential threat to national security as it encompasses the greatest amount of fissile material, whereas Categories II and III consist of smaller quantities. Both the Department of Energy and the NRC have implemented security programs specifically to address SNM. Each of these agencies has its own design basis threat [13, 14], a set of classified documents that assesses the technical, economic, and political components of an SNM threat and outlines the physical protection measures necessary to

counteract a threat. Additionally, other measures, such as inspection programs, reviews, performance tests, and detection systems have been deployed for further protection against potential nuclear attacks [14]. Border security is the most obvious mode of protection [15], but domestic monitoring of nuclear facilities, including physical protection and materials' accounting, are also important aspects of keeping nuclear materials secure [16]. In summary, greater focus on development of better, more efficient radiation detection technologies is crucial for securing ports-of-entry, government sites, and other sensitive locations.

1.2 Project Motivation and Objective

Neutron detection technologies are at the forefront of the effort to support the interdiction, search, and characterization objectives [17] of special nuclear materials. SNM emits neutrons and photons due to spontaneous and/or induced fission events. Though detection systems unique to each form of radiation (neutrons and photons) are widely available, various scintillators have been developed that are capable of simultaneously detecting gamma rays and neutrons and discriminating both forms of radiation. Signals detected by scintillators are characterized by fast and slow events, which cause prompt and delayed fluorescence respectively. The fraction of light in the slow component depends on the rate of energy loss, which is unique for each particle. Neutrons experience much slower energy loss than gamma rays, so their signal tails are distinguishable [18].

The objective of this thesis is to propose a new method of on-the-fly digital discrimination between neutrons and photons in scintillator detectors for the benefit of safeguards and other radiological applications. The solid-state scintillator studied in this research was the $Cs_2LiYCl_6:Ce^{3+}$ (CLYC) elpasolite [19], and the digitizer/signal processor used was the eMorpho [20]. The PSD method described herein was inspired by existing wavelet-based techniques [21], and also incorporates numerical integration methods.

1.3 Radiation Signatures of Fission Events

1.3.1 Spontaneous and Induced Fission

As mentioned previously, nuclear materials are fissile or fissionable. Hence, they are characterized by measurement of prompt and delayed neutrons and photons emitted in spontaneous or induced fission events. Passive neutron assay is the term used for detection of spontaneous events; it refers to a detection system or array placed near a potential spontaneous fission source [22]. High neutron and/or photon attenuation of suspect materials may prevent accurate assessment and characterization of material using passive assay techniques. In such cases, active neutron or photon interrogation is applied to create induced fission events by bombarding the sample with highly penetrating radiation beams [22]. SNM neutron emissions data [23] is provided in Table 2.

The natural decay process of spontaneous fission occurs in heavy nuclei as a result of competition between the nuclear force and Coulomb repulsion [24]. As the atomic number increases, the total nuclear force increases linearly with A. The Coulomb repulsion energy of the protons, however, increases at a rate proportional to Z^2 [24]. Thus, at higher atomic numbers, namely $A > 200$, the Coulomb repulsion becomes more prominent, increasing likelihood of nuclear instability. The propensity for nuclei to fission can furthermore be explained by thermodynamics. Heavy nuclei in the uranium range have a typical binding energy of ~7.6 MeV/nucleon [24]. When a heavy nucleus fissions into lighter nuclides of approximately half the original atomic number, the Coulomb barrier is overcome, and the binding energy per nucleon indicates that the product nuclides are more stable than the original nucleus.

Table 2: Neutron Emissions Data of Special Nuclear Materials

Nuclide	Spectrum Type	Total Neutron Yield, ν_t	Delayed Neutron Yield, ν_d
92-U-233	thermal	2.4968 ± 0.0036	0.0067 ± 0.0003
92-U-235	thermal	2.4355 ± 0.0023	0.0162 ± 0.0005
92-U-238	fast	2.819 ± 0.020	0.0465 ± 0.0024
94-Pu-238	fast	3.00 ± 0.14	0.0047 ± 0.0005
94-Pu-239	thermal	2.8836 ± 0.0047	0.0065 ± 0.0003
94-Pu-240	fast	3.086 ± 0.025	0.0090 ± 0.0004
94-Pu-241	thermal	2.9479 ± 0.0055	0.0160 ± 0.0008
94-Pu-242	fast	3.189 ± 0.035	0.0183 ± 0.0010

In order to achieve this more tightly bound state, energy must be released. This energy primarily takes the form of kinetic energy of the fragments, but can also be distributed among neutrons, β particles, and γ rays [24]. Higher decay probability is associated with larger energy release in fission because of the increased variety in energy distribution and final states.

Table 3: Binding Energy of the Last Neutron

Fissioning Nucleus ^{A}Z	Critical Energy, MeV	Binding Energy of Last Neutron in ^{A}Z, MeV
^{233}U	5.5	*
^{234}U	4.6	6.6
^{235}U	5.75	*
^{236}U	5.3	6.4
^{238}U	5.85	*
^{239}U	5.5	4.9
^{239}Pu	5.5	*
^{240}Pu	4.0	6.4

* These nuclei cannot be formed by the absorption of neutrons by the nuclei ^{A-1}Z.

Induced fission is an alternative route for materials that either lack the level of instability necessary for spontaneous fission or have low spontaneous signatures that can be enhanced by the input of energy. Induced fission occurs when the critical energy of fission [25] to overcome the Coulomb barrier is introduced by an external particle, most commonly by neutron absorption. When a neutron is absorbed, the compound nucleus rises to an excited state of an energy equal to the kinetic energy of the entering neutron plus its binding energy in the compound nucleus [25]. When the binding energy of the incoming neutron alone exceeds critical energy of fission, kinetic energy is not required for fission to be induced. See Table 3 [25] for critical energies of fission for special nuclear materials in MeV. One possible route for the induced fission reaction of ^{235}U by neutron absorption is provided below. It should be noted that the nucleus that actually fissions is ^{236}U.

$$^{235}_{92}U + ^{1}_{0}n \rightarrow ^{236}_{92}U \rightarrow ^{90}_{37}Rb + ^{143}_{55}Cs + 3n + Q \quad (1)$$

It is important to distinguish between the terms fissile and fissionable. Fissile nuclides can sustain a chain reaction with low energy or even zero energy neutrons [25], the latter viable when the rest mass of a neutron, 939.57 MeV, is sufficient to exceed the critical energy of the $^{A+1}$Z nucleus. Fissionable nuclides, on the other hand, require neutrons with sufficient kinetic energy to initiate fission [26]. In either case, fission immediately occurs upon absorption.

Table 4: Neutron Energies

Class	Energy	Description
Cold Neutrons	0 eV – 0.025 eV	Neutrons in thermal equilibrium with very cold surroundings
Thermal Neutrons	0.025 eV	Neutrons in thermal equilibrium with surrounding medium
Epithermal Neutrons	0.025 eV – 0.4 eV	Neutrons of kinetic energy greater than thermal
Cadmium Neutrons	0.4 eV – 0.5 eV	Neutrons of kinetic energy below Cd cut-off energy
Epicadmium Neutrons	0.5 eV – 1 eV	Neutrons of kinetic energy above Cd cut-off energy
Slow Neutrons	1 eV – 10 eV	Neutrons with kinetic energy in this range
Resonance Neutrons	10 eV – 300 eV	Neutrons whose probability of neutron capture exceeds the probability of fission; at specific energies (resonance peaks), the σ_a increases drastically
Intermediate Neutrons	300 eV – 1 MeV	Neutrons with kinetic energy in this range
Fast Neutrons (also Fission Neutrons)	1 MeV – 20 MeV	Neutrons of kinetic energy greater than 1 MeV
Relativistic Neutrons	$\geq$ 20 MeV	Neutrons in this high energy range

The most prominent particle emission due to fission is prompt neutrons, which are emitted instantaneously [25], in contrast to delayed neutrons, which are released after the fission event during the β^- decay of fission fragments. The average total number of neutrons released per fission for a particular isotope, denoted by the symbol ν, varies with the energy of the incident neutron. Prompt gamma rays are also emitted during fission [25], and they are distinguished from delayed gamma rays according to their release time.

1.3.2 Neutron and Photon Interactions with Matter

Neutrons interact with matter uniquely due to their lack of electric charge. There are two primary interaction mechanisms, scattering and capture, which depend on the kinetic energy of the incident neutron. See Table 4 [26] for energy classification of neutrons. Scattering, which can be elastic or inelastic, dominates at high kinetic energy, whereas radiative capture dominates at low kinetic energy. The likelihood of either interaction depends on the microscopic cross section σ [27], which describes the probability of interaction in barns (cm^2). Different types of interactions exist for a given target material. The sum of microscopic cross sections is the total probability of any kind of interaction with a nucleus, as shown in Equation 2. When the target material is mixed, microscopic cross sections for these materials must be considered through the use of the macroscopic cross section, shown in Equation 3.

$$\sigma_t = \sigma_e + \sigma_i + \sigma_\gamma + \sigma_f + \cdots \quad (2)$$

[t = total, e = elastic, i = inelastic, γ = gamma/photon, f = fission]

$$\Sigma = n\sigma \quad (3)$$

[n = density of nuclei]

Neutrons are attenuated in matter in a manner related to the absorption cross section. Equation 4 relates the incident beam intensity and the intensity remaining after the neutron beam transports through a finite distance of material.

$$I(x) = I_0 \cdot e^{-\sigma t n x} \quad (4)$$

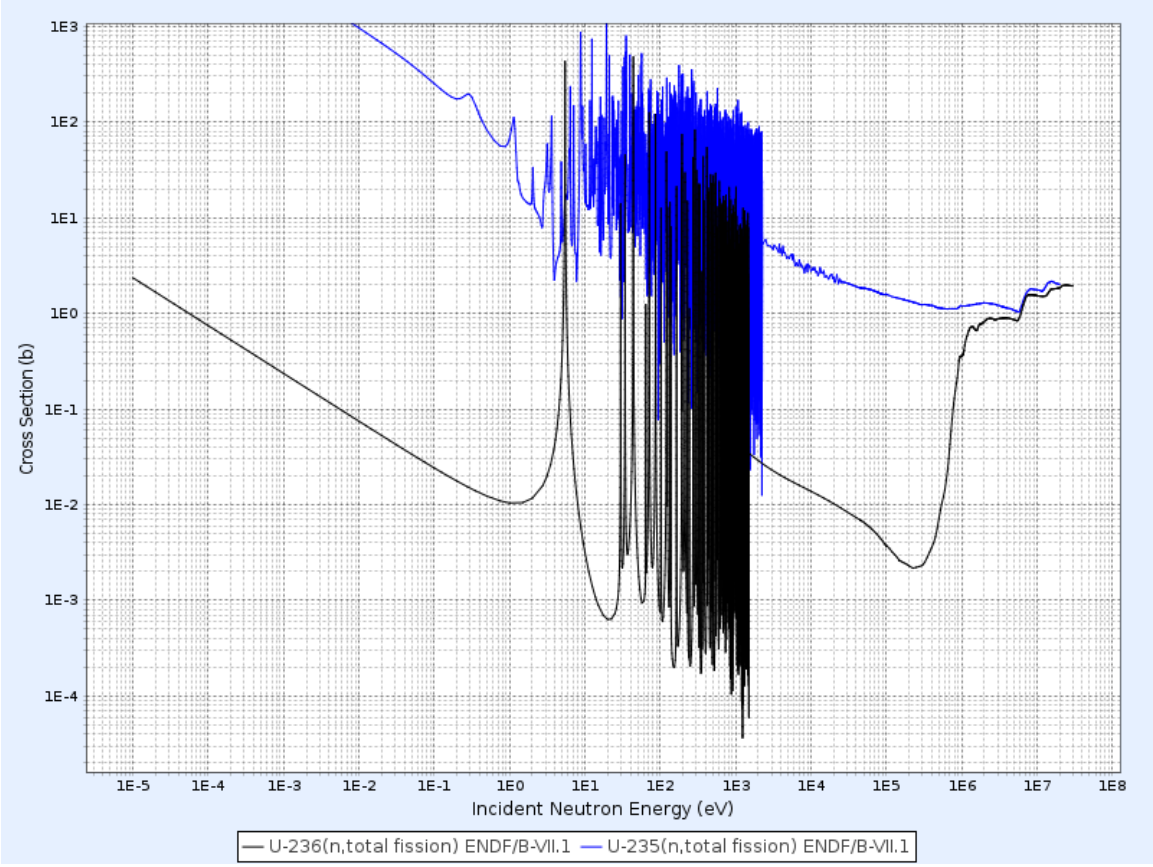

Figure 1: Fission Cross Sections of U-235 and U-236

Gamma rays, on the other hand, are electromagnetic radiation caused by nuclear transitions. Unlike neutrons, photons interact with the electromagnetic fields (i.e., electrons) of atoms. Photons can undergo three interaction mechanisms with matter, depending on the energy of the incident radiation and the type of material in the target: the photoelectric effect, the Compton effect, and pair production. Figure 2 [28] illuminates the dominant interactions for incident photon energies and the atomic number of the absorbing material.

The *photoelectric effect* occurs when a low-energy photon interacts with an atom. It completely transfers its energy to an atomic electron and disappears. The photoelectron is ejected from the atom with an energy equal to the difference between the energy of the incident photon and the

binding energy of the electron [29]. If the source of the photoelectron is not the outer shell, electronic reconfiguration occurs; an outer shell electron drops to a lower level to fill the vacancy. This transition causes characteristic x-ray emission or ejection of an Auger electron [29].

The *Compton effect* is the most likely interaction for mid-high energy range of incident photons. Compton scattering occurs when the incident photon collides with an atomic electron, scattering through some angle θ [29].

Lastly, *pair production* occurs at high incident photon energies. In this case, the photon nears the Coulomb field of an atom and materializes into a positron and an electron pair. This is a threshold process requiring 1022 keV. The positron slows down and annihilates with another electron in the medium, releasing two 511- keV gamma rays.

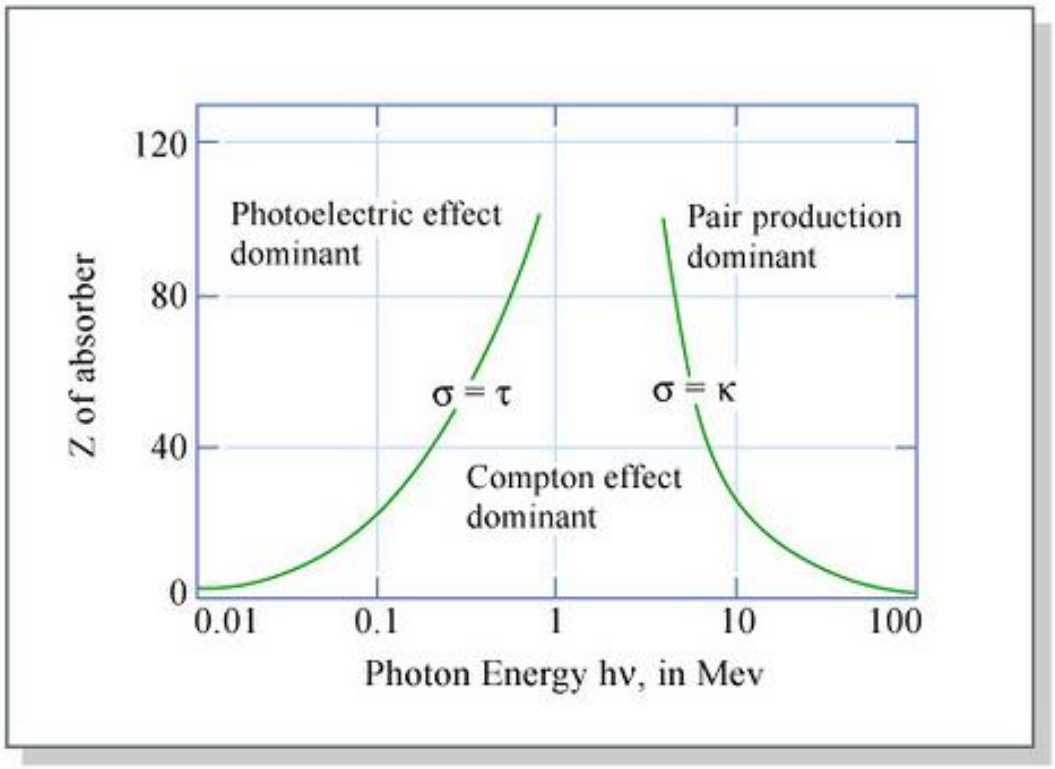

Figure 2: Photon Interactions with Matter

Interactions of neutrons and photons with matter is the basis for the radiation detection technologies. Photons, as explained above, interact directly with electrons; when gamma radiation interacts with a detector, such as a gas-filled detector or proportional counter, ionization immediately occurs and electric current is generated. Neutrons, however, interact with a detector material via two major mechanisms: recoil and capture. Recoil occurs when a neutron scatters off a nucleus, which causes charged particles (protons) to recoil with subsequent ionization of the surrounding material [30]. The other mechanism, neutron capture, causes a nuclear reaction that produces charged particles (i.e., protons, alpha particles, or fission fragments), which can cause ionization that generates current in a detector that can be processed using analog or digital electronics.

CHAPTER 2 – LITERATURE REVIEW

2.1 Review of Radiation Detection Data Analysis Methods

2.1.1 Overview of Pulse Shape Discrimination Techniques

Different types of radiation, namely neutrons and photons, produce different pulse shapes due to their unique interactions with scintillators. The primary factor causing different pulse shapes is the time profile of the current produced [31]. Pulse shape discrimination thus employs computational methods to exploit these characteristic shapes and categorize them appropriately. Methods of pulse discrimination differ depending on whether the pulses are analyzed on the fly, i.e. on board the detector, or upon transfer to another computer.

Several conventional and digital pulse discrimination methods exist and are currently in use. They can be categorized on the basis of their implementation: time domain only or time and frequency domain. Time domain methods rely on specific time, relative to peak time and amplitude, making it "more sensitive to noise and light intensity" [31]. Frequency domain methods apply frequency transform methods to create a set of coefficients that can be analyzed for discrimination. A brief overview [31] of some currently used PSD methods is provided to show some of the variety in mathematical technique:

Rise time discrimination method (RTD) and *charge comparison method* (CCM) both require pulse integration for analysis. These methods measure the entire charge integration against the partial charge integration of either the rise or tail of the pulse and use the ratio of one against the other as an identifying feature of the pulse.

Pulse gradient analysis (PGA) measures the gradient of pulse tails. The trailing edge of a neutron pulse has a shallower gradient than that of a photon pulse [32]. An identifying threshold

value is defined by finding the ratio of the pulse's relative height in the trailing edge with a pulse peak so that anything above the threshold value is one type of radiation, whereas a pulse with a value lying below the threshold is defined as another type of radiation.

Zero crossing method (ZCO) is specifically used to discriminate bipolar pulses, which have unique zero-crossover points that depend on pulse shape and rise time. Prior to analyzing for the zero-crossover, the pulses must individually be passed through a "shaping network" [31].

Frequency gradient analysis (FGA) involves applying a Fourier transform to the signal. The zero-frequency and first-frequency components are extracted and used to define a discrimination parameter. FGA is insensitive to pulse response variations of a photomultiplier tube [33] and has the potential to be used in embedded electronic systems for on-the-fly analysis.

Principal component analysis (PCA) uses an algorithm that applies orthogonal transformation to a set of scintillation pulses in a matrix. The pulses are converted into coefficients called principal components, from which their eigenvectors are analyzed to identify unique differences [33]. Since PCA is applied to a set of pulses, it cannot be implemented in embedded electronics for real-time analysis.

2.1.2 Review of Discrete Wavelet Transform and Haar Wavelet

The methods described in the previous section are some of the more common techniques used for pulse discrimination. The method used in this study actually combines ideas from *rise time discrimination*, *charge comparison*, and *pulse gradient analysis* with a mathematical technique called the discrete wavelet transform for a more accurate method of pulse shape discrimination.

The discrete wavelet transform is one of many transformations that can be applied to a raw signal for the purpose of extracting information that is not necessarily apparent. It passes the raw,

time-domain signal through a series of varying high-pass and low pass filters, which extracts the high-frequency and low-frequency information from the signal [34]. These filters are applied in windows sampled for every spectral component, which vary over the signal. The discrete wavelet transform is defined as follows:

$$\mathrm{W}(\tau,\mathrm{s}) = \psi\,(\tau, s) = \frac{1}{\sqrt{|s|}} \int x(t)\,\psi^{*}\,\frac{t-\tau}{s}\,dt = \int_{-\infty}^{\infty} f(x)\psi^{*}{}_{\tau,s}(x)dx \tag{5}$$

$$f(x) = \frac{1}{E_{\psi} s^{2}\sqrt{s}} \iint_{-\infty}^{\infty} \mathrm{W}(\tau,\mathrm{s})\,\psi^{*}{}_{\tau,s}(x)\,d\tau\,ds \tag{6}$$

As shown above, the transformed signal is a function of two variables, τ and s, which stand for translation and scale, respectively [34]. The translation parameter refers to the movement of the window, which continuously shifts over regions of the signal. The scale parameter refers to the level of detail chosen for the transform in each window; it is the inverse of the frequency at which the wavelet is applied in a single window. The mother wavelet is represented by ψ^{*}. Literally, a 'wavelet' is just a small wave [34], and 'mother' indicates that the given wavelet serves as a template for producing the functions applied in each window. The star* indicates normalization.

The wavelet is initially set at the beginning of the signal or time t = 0. The product resulting from the wavelet function at some defined scale, s = 1 in the case of this study, and the signal is then integrated over all time. The resulting number is then multiplied by the constant term $\frac{1}{\sqrt{|s|}}$, and the value is saved as the coefficient representing the wave at t = 0 and s = 1. The wavelet window at scale s = 1 is then shifted by τ, and the above process is repeated to produce a coefficient for t = τ and s = 1. The process is repeated for the entire signal. Lastly, s is increased by a small

amount, and the procedure is performed again. The result of this process is a set of detail and approximation coefficients, which together are called frames.

The mother wavelet used in this study is the Haar wavelet [35]. It is a step function of with $2M$ subintervals of length $\Delta x = (B - A)/(2M)$. The first eight Haar wavelets are illustrated on the in Figure 7. Note that i = 1 is invalid; it is a box rather than a step function wave. The i'th Haar wavelet is defined (Eq. 7) under the following conditions: $i > 2$, $\mu = \frac{M}{m}$, $\xi_1(i) = A + 2k\mu\Delta x$, $\xi_2(i) = A + (2k + 1)\mu\Delta x$, and $\xi_3(i) = A + 2(k + 1)\mu\Delta x$.

$$h_i(x) = \begin{cases} 1 & for\ x\ \epsilon\ [\xi_1(i), \xi_2(i)), \\ -1 & for\ x\ \epsilon\ [\xi_2(i), \xi_3(i)), \\ & 0\ elsewhere \end{cases} \tag{7}$$

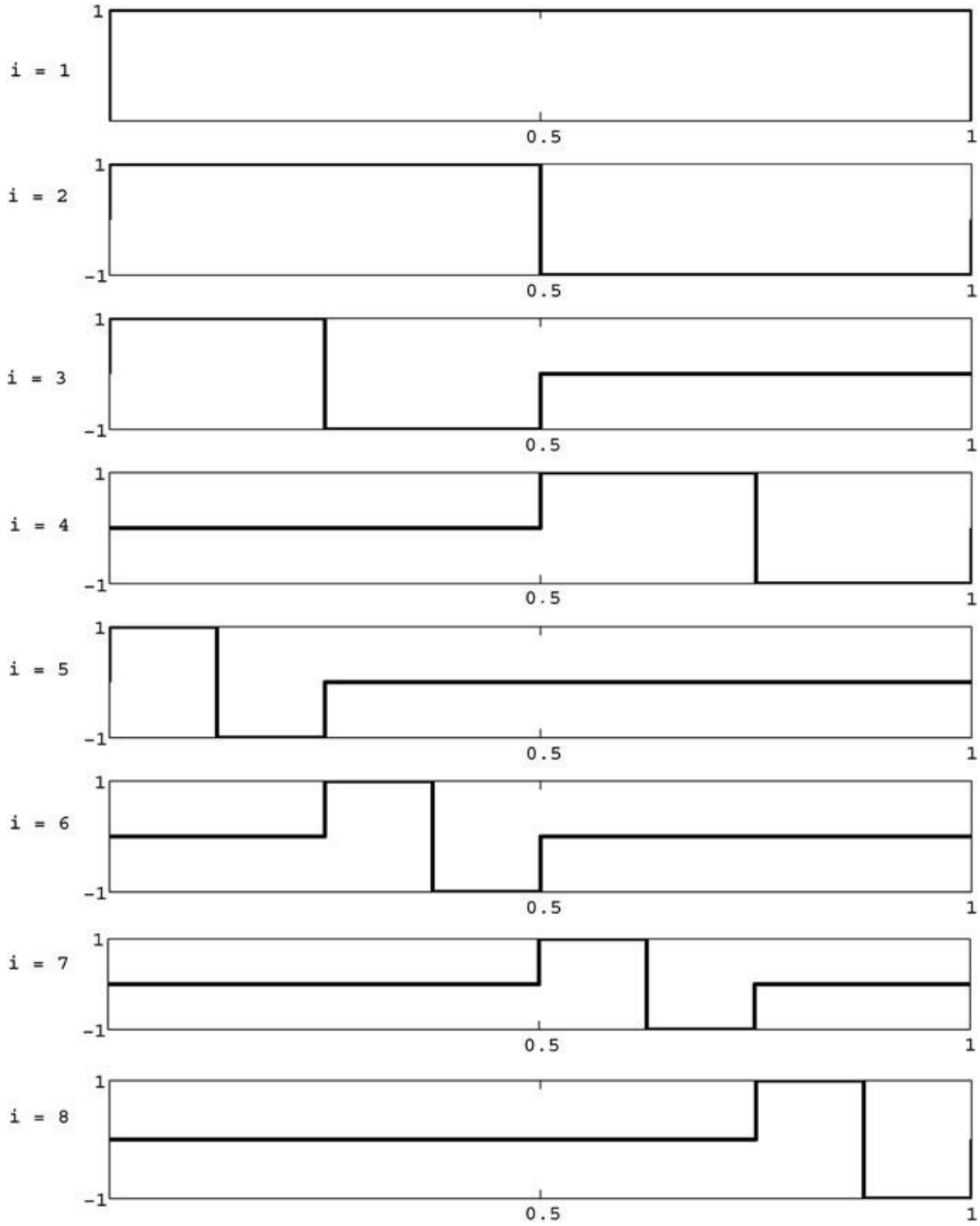

Figure 3: The First Eight Haar Wavelets

2.2 Quantification of Pulse Discrimination Techniques

When a new pulse discrimination method has been developed, its accuracy can be visually evaluated with a scatter plot; the radiation identification values for each signal are plotted against the total integral under the power of the waveform, which represents energy or power of the pulse or a related quantity. Neutron and gamma-ray signals recorded by a single detector are thus evaluated with the PSD method and a plot is generated simultaneously with two distinct regions which ideally have no overlap.

Each region is fitted to a Gaussian distribution centered about the average radiation identification value (RID) for neutron and photon, respectively [36]. The σ parameter of the Gaussian is calculated for both the neutron and photon regions so that the figure of merit (FOM) can be calculated [37]. Below are equations for Gaussian fit and figure of merit. The term X is the mean value of x, the RID sample input.

$$G_{X,\sigma}(x) = \frac{1}{\sigma\sqrt{2\pi}} e^{-(x-X)^2/2\sigma^2} \tag{8}$$

$$FOM = \frac{|X_{neutron} - X_{photon}|}{2\sqrt{2\,ln2}(\sigma_{neutron} + \sigma_{photon})} \tag{9}$$

CHAPTER 3 – Experimental Measurements

3.1 Radiation Measurements Using Scintillation Detectors

3.1.1 Mechanism of Scintillation

Scintillator detectors, unlike their gas-filled predecessors, are typically composed of solid material (liquid scintillators also exist) [39]. Solid state scintillator detectors are advantageous because, due to their higher densities, they have better efficiency for gamma-ray interactions. Solid state detection medium is preferable for real world applications. They are rigid, non-toxic, and non-flammable. The energies of radiation interaction can be measured, which allows for radiation source characterization or the differentiation between scattered and un-scattered particles.

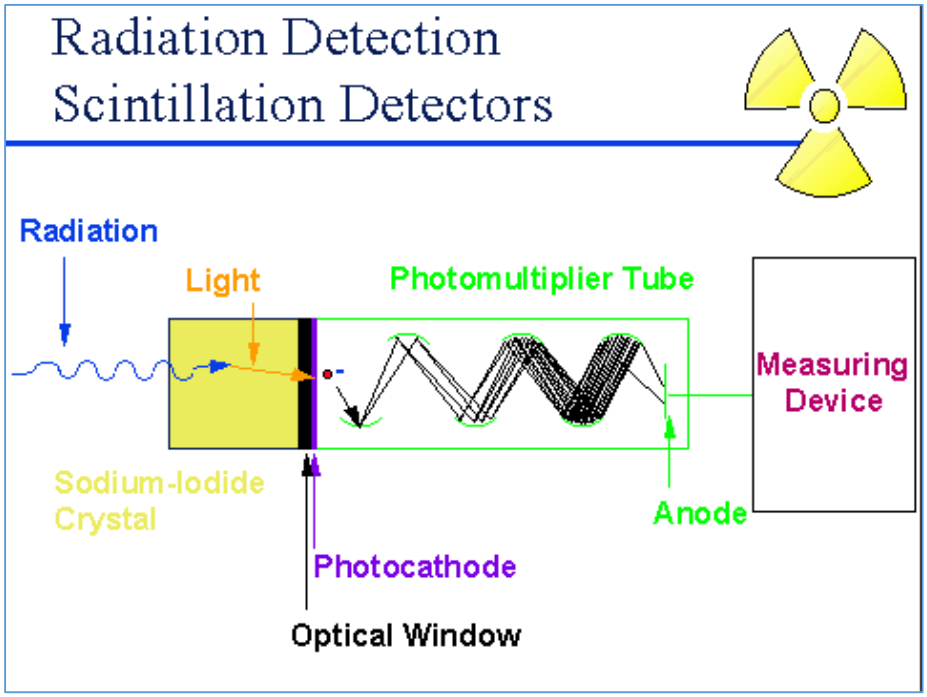

Figure 4: Scintillator Detector Scheme

Scintillation refers to the process of giving off light, so a scintillator is "any material that can release a photon in the UV or visible-light range, when an excited electron in the scintillator returns to its ground state" [39]. The scintillation photons can be collected using an optical read-out such as a photomultiplier tube (PMT) or solid state silicon photomultipliers (SiPM). It collects the scintillation photons at a cathode and translates them into an electric signal. See Figure 3 [40] for a diagram. Two conditions must be satisfied for a solid state detector: 1) the materials must be optically transparent and have little background noise in the absence of radiation, and 2) electrons and ions must be able to be transported through it [41].

Several materials are able to scintillate. Among the most cost-effective are organic scintillators, which often contain conjugated ring compounds. The interaction between molecules within organic compounds are relatively weak, and they have two modes for absorbing energy: they can undergo excitation and they can vibrate against each other [41]. While excitation usually occurs at a few eV, vibrational energies only amount to ~0.1 eV, as the iterative interaction causes loss of a few eV each time. Upon excitation, the molecule will decay down to its lowest vibrational state, and furthermore to its ground state.

Inorganic scintillators are composed of materials with much higher atomic number and density [40] than organic scintillators, including, but not limited to, bismuth germinate, lutetium oxyorthosilicate, and gadolinium oxyorthosilicate. The larger density allows for an increased energy capacity – thus high energy radiation can be sufficiently processed and detected with inorganic scintillators. However, this broader range in energy comes with a price. Scintillation crystals such as NaI, in particular, are manufactured to such "exacting tolerances" [40], that they must be handled with great care; their hygroscopic nature requires hermetic sealing so that moisture is not absorbed, destroying the crystal's properties. Another notable characteristic of

some inorganic, crystal scintillators is their fortification with activators, which provide states in the energy gap between activated and excited states of the other material [41].

For organic and inorganic scintillators alike, decay time is a crucial characteristic because it denotes the length of time that scintillation photons are emitted after a radiation interaction [40]. The length of decay time determines the ease discrimination between radiation types as well as what modes the detector will primarily be operated in.

3.1.2 CLYC Scintillator

An inorganic scintillator composed of the elpasolite Cs_2LiYCl_6 (CLYC) was used in the detector system for this study. The solid state CLYC is attractive for applications in portable detection systems due to its ability to simultaneously detect photons and neutrons [42]. Neutrons have been conventionally detected with solid state scintillators activated with ^{3}He, ^{6}Li, and ^{10}B, which have high neutron absorption cross sections at low energies; for fast neutrons, detection systems have been constructed with ^{1}H scattering or moderators to slow them down to thermal energies [43]. The CLYC crystal's composition has ^{6}Li for thermal neutron absorption, but also boasts a new method for fast neutron detection using ^{35}Cl [44]. The reactions are shown below:

$$ {}^{1}_{0}n + {}^{6}_{3}Li \rightarrow {}^{3}_{1}H + {}^{4}_{2}He \tag{10} $$

$$ {}^{1}_{0}n + {}^{35}_{17}Cl \rightarrow {}^{35}_{16}S + {}^{1}_{1}p \tag{11} $$

In the thermal reaction, the Q-value is 4.78 MeV, shared by the alpha particle (2.05 MeV) and triton (2.73 MeV). The fast reaction has a Q-value of 0.615 MeV, which entirely goes to the proton in addition to the incident neutron energy [44].

The CLYC crystal has three light decay times: 1, 50, or 1000 nanoseconds [44]. Its light yields are 73,000 photons per thermal neutron and 22,000 photons per 1-MeV gamma ray [42, 43]. The CLYC's energy resolution is a remarkable 3.9% FWHM and 662 keV [42], compared to NaI crystals which have resolutions of 7.5% FWHM at 662 keV [43].

Figure 5: CLYC

Figure 6: High Voltage Base

3.2 Optical Readout

3.2.1 Mechanism of Photomultiplier Tube

As mentioned previously, the scintillation photons need to be converted into an electric signal [39]. The photomultiplier tube is a standard device of optical readout. There are several components to a PMT: the photocathode, the focusing grid, a series of dynodes, and a high-voltage power supply. In the detector assembly, as shown in Figure 3, the photocathode lies flush with the scintillator. The photocathode is a thin layer of photo-emissive material – it emits electrons when struck by photons [39]. Photoemissive materials are typically metal alloys like K_2CsSb and Na_2KSb, which have electrons to spare. Once electrons have been emitted by the photocathode, the focusing grid applies an electric field to channel the electrons toward the first dynode. The PMT must be in vacuum, as well as be contained in housing as shown in Figure 5 [45] that protects against outside electric or magnetic fields.

Figure 7: Hamamatsu Photomultiplier Tubes

The series of dynodes is merely a chain of electrodes, similar to the photocathode. They are likewise made of metal alloys that have a "high probability of secondary electron emission" [40] and multiply the number of initial electrons. The high voltage, accompanied by a series of voltage dividers, sets the potential difference between adjacent dynodes at a few hundred volts. The electrons thus accelerate towards each of these with ~100 eV of energy. Some energy is consumed when releasing the electrons from the dynode, however, so gain is limited at 30 – 50 eV in total. For those that actually release at the surface of the dynode and make it to the next dynode, gain is realistically around 5 eV [40]. Each PMT contains 8 – 12 dynodes, for a total multiplication factor of around 10^6. At the end of the dynode chain is an anode, which collects all electrons and produces the electric signal.

Figure 8: Hamamatsu Photomultiplier Tube Housing

3.2.2 Hamamatsu Photomultiplier Tube

The photomultiplier tube used in the CLYC detector assembly was the Hamamatsu R6231-100 tube [46], shown in Figure 6. Its outer diameter is 51 mm, and the diameter of the photocathode effective area is 46 mm. Inside are 8 dynode stages, and the maximum voltage from anode to cathode is 1500 V, with a supply voltage of 1000 V. Typical gain is 2.3×10^5 at the anode.

Other features include a spectral response of 300 – 650 nm and a minimum luminous sensitivity of 110 µA/lm. A typical rise time (the time to reach the waveform maximum) is 8.5 ns, with a total transit time of 48 ns.

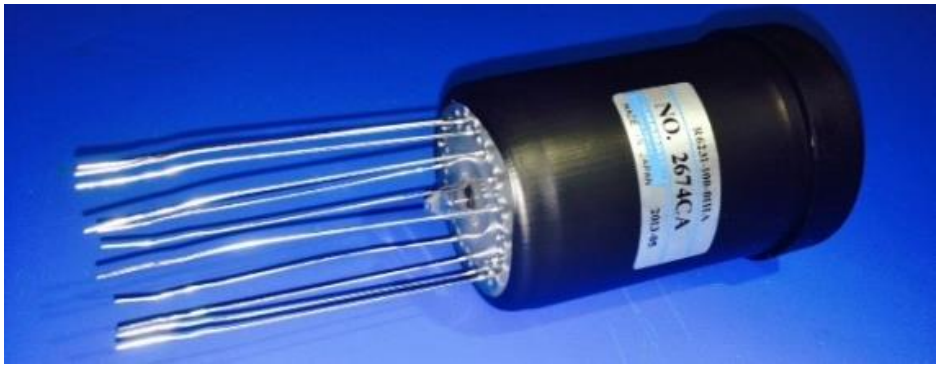

Figure 9: Hamamatsu R6231-100

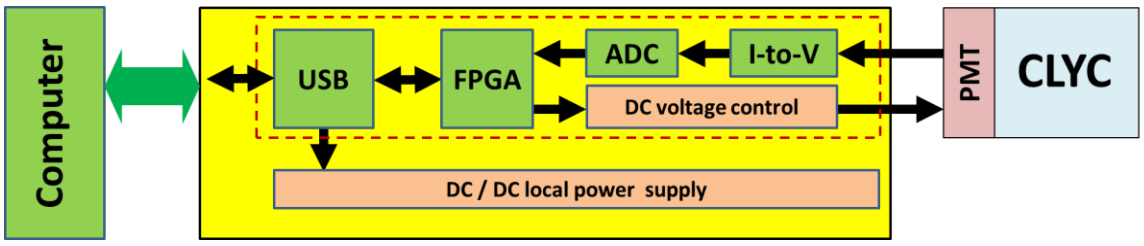

Figure 10: Detector Assembly Scheme

3.3 Signal Processing

3.3.1 Signal Analyzers

Despite amplification from the dynode chain in the photomultiplier tube, the signal output of the anode is still small against the PMT's intrinsic noise. In many detectors, this issue is solved by attaching a preamplifier directly to the PMT. The preamplifier not only increases the signal strength by a factor up to 100, but also lengthens decay time thereby extending the pulse tail before passing the signal to the remaining electronics [47].

The next step is signal processing in the pulse height analyzer (PHA), which measures the pulse amplitude. This can either be a single channel analyzer (SCA) or a multichannel analyzer (MCA), the only difference between the two being stringent, operator-set limits on the SCA [47]. The PHA extracts energy information from the voltage signal, and the accepted pulses are recorded by the scaler/timer. When using an SCA, events outside the set range are rejected. An MCA, however, digitizes the entire PMT output into one of several channels, and then displays all radiation events in a pulse-height spectrum. The horizontal axis of a pulse-height spectrum represents a narrow range of pulse heights, whereas the vertical axis represents the event count at that pulse height. See Figure 6 [47] for an example of an MCA pulse-height spectrum readout.

3.3.2 eMorpho Digitizer

The CLYC detector assembly included the eMorpho, a digitizer/MCA unit which does not require a preamplifier due to its internal and buffer amplifiers, the latter which restricts bandwidth [48]. The data stream is processed in real-time by a field programmable gate array (FPGA) which communicates with a computer via USB.

CHAPTER 4 – COMPUTATIONAL ANALYSIS

The waveforms were collected using the CLYC-eMorpho detector system, identified visually with Igor Pro software, and then saved as text files. Twenty digitized waveforms each of neutrons and photons were initially analyzed and compared in Matlab, and a signal identification scheme was coded using the wavelet transform.

Following the scheme in Figure 11, the text file input of the signal is uploaded to the directory and saved as a vector. The discrete wavelet transform is applied to the vector, producing two levels of coefficients, the approximation coefficients and the detail coefficients. The approximation coefficients represent the de-noised version of the original signal, or the *approximation* of the signal. The detail coefficients, on the other hand, represent the deviation of raw values from the approximated signal, and thus are not useful for pulse discrimination purposes.

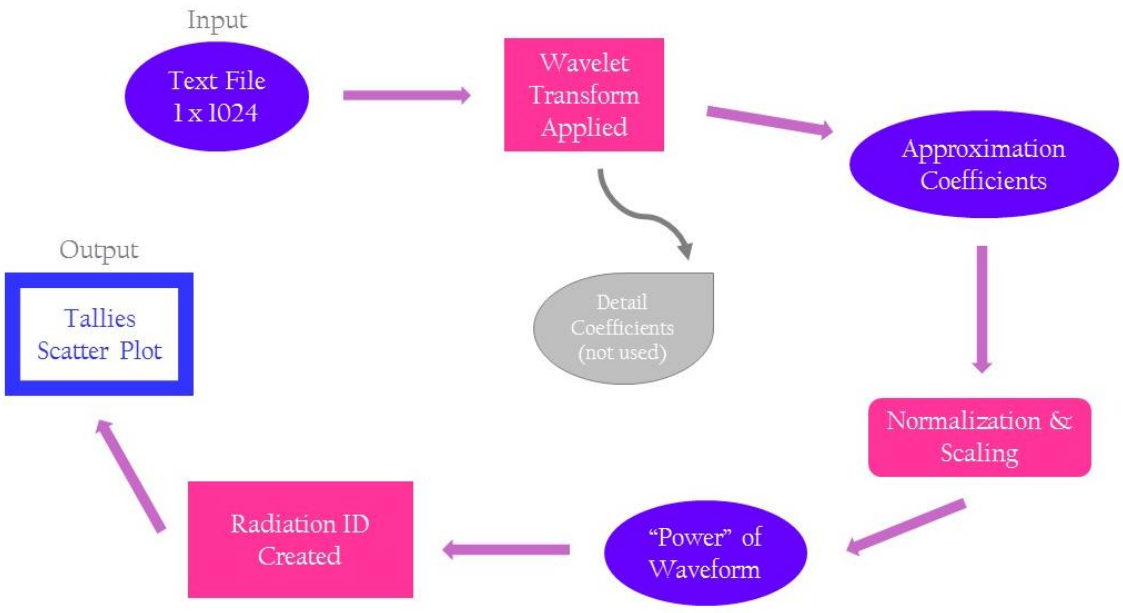

Figure 11: Scheme of Waveform Processing

The approximation coefficients are normalized as a vector and scaled down so that the baseline is flush with the x-axis. The wave vector is then transformed into a power function via the following equation:

$$P(\mathrm{W}) = \frac{|\mathrm{W}(\tau, \mathrm{s})|^2}{\sqrt{2\pi}} \tag{12}$$

The power is calculated to exaggerate the defining characteristics of the wave so that feature extraction more apparent. As shown below in Figure 12, the tail of the neutron waveform power has greater breadth, whereas the gamma-ray waveform power is narrower with a much steeper slope. This is also true of the waveforms themselves, but to a lesser extent. Another function that also exploits these characteristics could be used – power has physical merit and has been used previously in wavelet analysis in PSD methods [22].

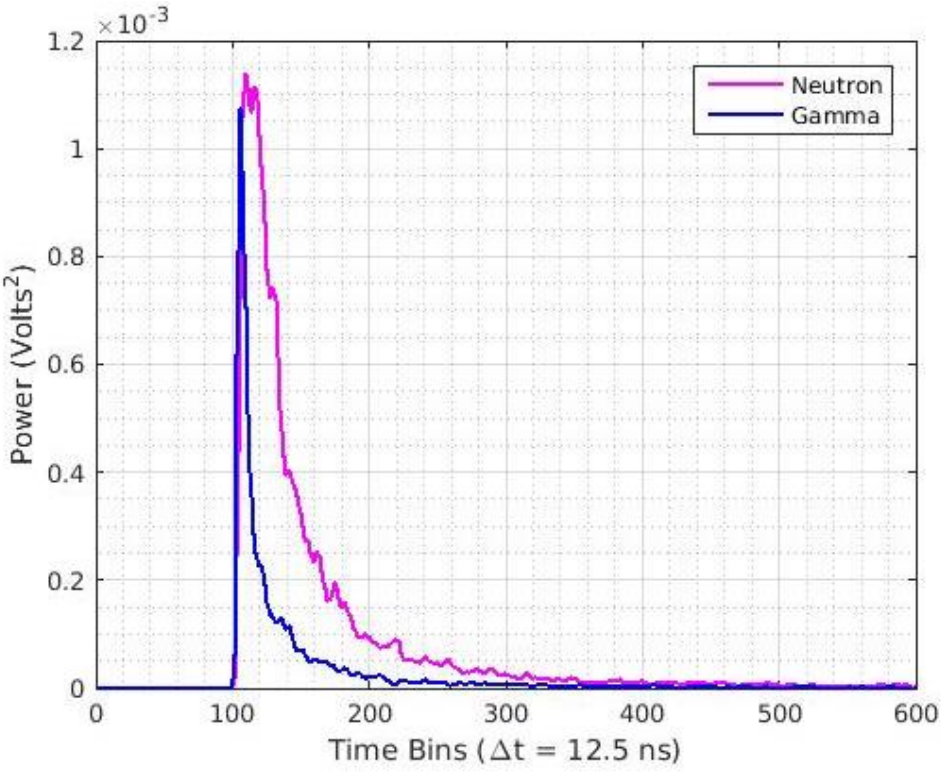

Figure 12: Power of the Waveform

The integral is calculated with a trapezoidal function, and the radiation identification value is calculated from partial integration over preset time ranges. The RID value for neutrons is larger than that for gamma rays, so a threshold parameter is set so that incoming radiation is categorized as either a neutron or a gamma ray. A study was conducted to determine the ideal time frame for partial integration of the power of the waveform. As illustrated in the diagram in Figure 11, the time scale for the signal has 1024 bins of 12.5 nanoseconds, but even in the truncated powers of the waveforms in Figure 12, one can see that tails bear no distinguishing characteristics beyond 300 bins. The region of interest lies between the rise time and the decay of the pulse, around 100 – 300 bins.

CHAPTER 5 – RESULTS

5.1 Pulse Shape Discrimination

Including the forty waveforms used to determine the threshold for RID values between neutrons and photons for the CLYC detector, a total of 505 waveforms were analyzed using the computational method described in the previous chapter. Their discrimination is illustrated in the scatter plot in Figure 13. The x-axis represents the RID value, and the y-axis represents the corresponding full integral of the power of the signal with units of Volts^2·nanoseconds. The dashed line (the threshold between neutrons and photons) in Figure 13 at the value of 0.865 represents the boundary implemented for identifying the radiation type.

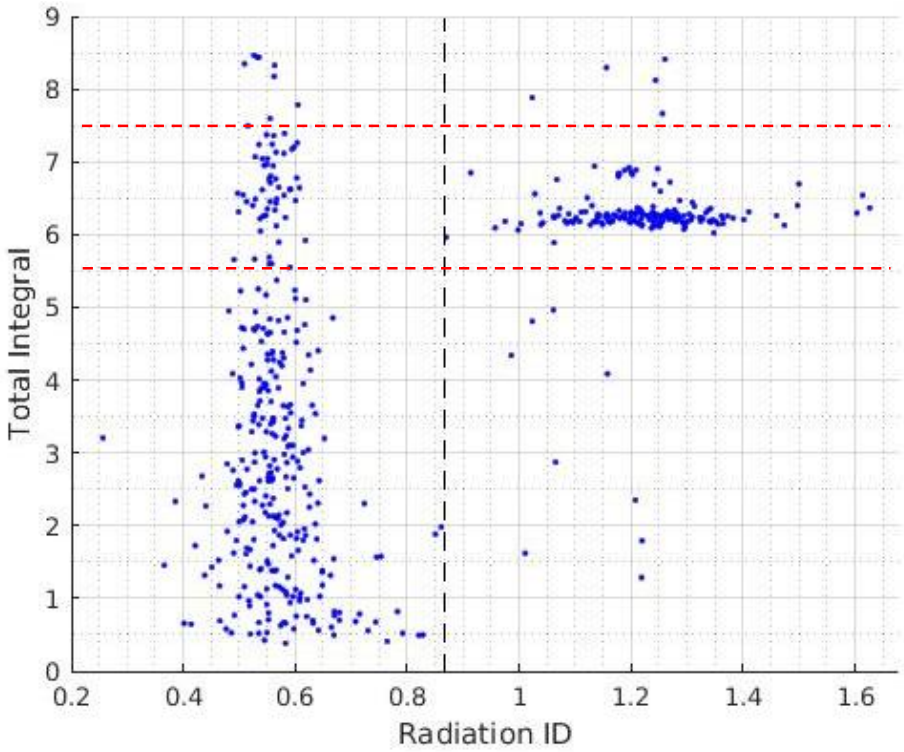

Figure 13: Scatter Plot of Total Integral vs. RID

The points in the plot with RIDs greater than the threshold have been identified as neutrons, and those less than the threshold are gamma rays. It was determined that the CLYC detector enables excellent PSD properties. The analysis of a few waveforms, however, generated borderline RID values, as shown in the scatter plot as well as the histogram depicted in Figure 14. Most of the points nearest the threshold are gamma rays with low total integrals, which correspond to their low energy. This follows from a decreased amplitude of the waveform which moderates the slope of the gamma tail. The analysis attempts to exploit the steepness of the gamma-ray signal tail relative to the neutron signal tail, so diminishment of this feature could result in misidentification.

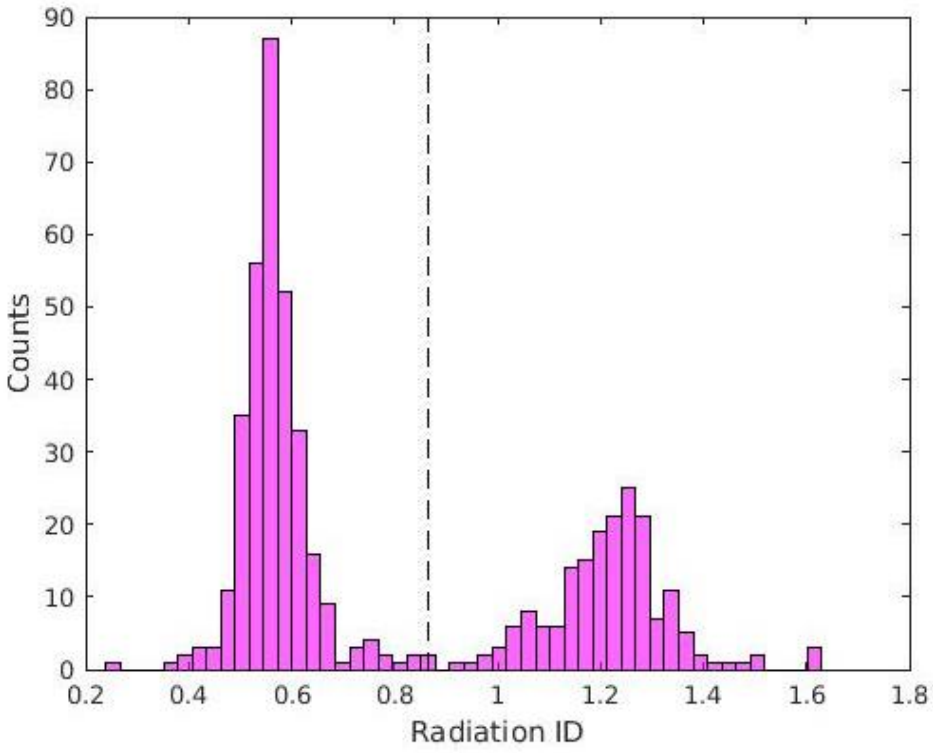

Figure 14: Radiation Identification Frequency

Table 5: Gaussian Fits

	Total Number N	**Mean X**	σ	$FOM = 1.75$
Neutron	182	1.2184	0.1178	
Gamma	323	0.5669	0.0686	

The mean and standard deviation values were calculated for Gaussian fits of the RID value distributions for neutrons and gamma rays. This information was used to calculate the figure of merit for the PSD [39]. The figure of merit (Table 5) for separation between neutrons and photons for the CLYC detector using the developed technique is 1.75. In any dataset, the FOM is dependent on the following [39]:

a) the waveform amplitude range, which corresponds to the energy of the waveform – the total integral of the waveform power in this case; and
b) the number of radiation quanta analyzed.

The Pu/Be source produced many more photons than neutrons. The detector registered approximately 8 – 10 times as many photons as neutrons. The number of waveforms for each type of radiation saved for this analysis was affected by this bias, but effort was made to save enough neutrons to compensate for some of this discrepancy. As shown in Table 5, compared to the number of neutron waveforms, less than twice as many gamma-ray waveforms were collected.

The variation in waveform energy was large for the gamma-ray waveforms, but small for the neutrons, as shown in the scatter plot (Figure 13). The scaled total integral values of the power vectors created after vector normalization of the wavelet coefficients span a much greater range for gamma rays than for neutrons. The RID integrals for gamma rays span the approximate vertical range of 0.5 – 8.5, whereas the density of the RID integrals for neutrons is primarily concentrated in the range of 5.5 – 7.5. If limits are applied in the computational analysis to exclude any points

with integrals outside the range designated by the dashed red lines in Figure 13, the figure of merit will improve. These lines represent the region of interest for the neutrons from the mixed Pu/Be source. The total integral, as mentioned previously, is representative of the waveform power and furthermore the energy. A given source will have its own typical neutron emission energies, so setting limits to analyze a specific energy range is common practice.

5.2 Error Analysis

The primary source of error in creating the RID is the wavelet decomposition. The wavelet transform de-noises/compresses data by approximation, so error is intrinsic to the process. In the second chapter of this thesis, it was mentioned that a scaling function is used through the projection [49]. These coefficients are defined in Equation 13.

$$c(\tau, s) = c_{\tau,s} = < f(t), \psi^*{}_{\tau,s}(t) > = \frac{1}{2^{\tau/2}} \int f(t)\psi^*(2^{-\tau}t - s)dt \tag{13}$$

It is the approximation from this scaling that produces the error in the sets of coefficients (frames). Scaling can occur on multiple levels, i.e., s = 1, 2, 3…etc., but in this study, only a first level decomposition was considered. The mean square error of the approximation coefficients and scaling functions are expressed in Equations 14 and 15 [49].

$$E_{\psi}^{N} = \int [\psi_{N}^{\infty}(t) - \psi_{L}^{N}(t)]^2 dt \tag{14}$$

$$E_{\psi^*}^{N} = \int [\psi^*{}_{N}^{\infty}(t) - \psi^*{}_{L}^{N}(t)]^2 dt \tag{15}$$

The term N is the number of taps [49], which is specific to the mother wavelet chosen. The Haar wavelet has two taps. The term L is half the length of the digital waveform. The radiation input files are 1024 units in length, so L is 512. The total error can be simplified; the normalized mean square error for K total coefficients (1024) between $f(n)$ and $c(n)$ is defined in Equations 16 and 17 [49].

$$e(n) = |f(n) - c(n)| \tag{16}$$

$$e_{mse} = \frac{1}{K}\sum_{n=1}^{K}\frac{[e(n)]^2}{[f(n)]^2} \tag{17}$$

In summary, the error of a single waveform is calculated as follows: the square of the difference between each frame (the approximation coefficient and its corresponding detail coefficient) is summed, and this sum is divided by the total number of frames for the waveform.

CHAPTER 6 – CONCLUSIONS & FUTURE WORK

6.1 Conclusions

A new method of on-the-fly discrimination between neutrons and photons was developed for the CLYC elpasolite detector. This work demonstrates that wavelet decomposition can be used with other numerical techniques to construct a radiation identification scheme that fully separates radiation types measured by a single detector simultaneously.

6.2 Future Work

There are several possibilities for future work based on this research:

- Increased levels of decomposition could be studied and compared to the first level decomposition.
- The Matlab code could be converted into a universal programming language such as C or C++ and uploaded to the FPGA module of the eMorpho digital analyzer. This would enable on-board discrimination of radiation.
- The method could be tested with other scintillator detectors. This would require resetting parameters according to the unique time profiles of the scintillator signals.
- Furthermore, though this method is specific to neutron and gamma ray discrimination, a similar technique could be applied to any other radiation combinations measured with a single detector with unique time profiles.

REFERENCES

[1] Radiation Detection Technologies, Inc. 'Applications', 2016. [Online]. Available: http://radectech.com/neutron-detection-applications. [Accessed: 3-April-2016].

[2] P. Lecoq, "Spin-off from particle detectors in the field of medicine and biology," *Nuclear Instruments and Methods in Physics Research Section A*, 2007, pp. 1 – 11.

[3] Science Daily, Oak Ridge National Laboratory, 'Neutron detector will advance human disease research', 2012. [Online]. Available: https://www.sciencedaily.com/releases/2012/09/120906154220.htm. [Accessed: 2 – April – 2016].

[4] H. Berger, *Corrosion Monitoring in Industrial Plants Using Nondestructive Testing and Electrochemical Methods*, Montreal, Canada: ASTM Special Technical Publication, 1984, pp. 1-14.

[5] A. V. Da Rosa, *Fundamentals of Renewable Energy Processes*, 3rd Edition, Waltham, MA: Elsevier, 2013, pp. 809-815.

[6] IAEA Safety Standards, 'Radiation Protection Aspects of Design for Nuclear Power Plants', 2005. [Online]. Available: http://www-pub.iaea.org/MTCD/publications/PDF/Pub1233_web.pdf. [Accessed: 3-April-2016].

[7] "World Nuclear Weapons Stockpile Report," Ploughshares Fund, 23 June 2015, www.ploughshares.org. [Accessed: 24-Jan-2016].

[8] Ploughshares.org, 'Iran in Nuclear Compliance: Implementation Day is Here', 2016. [Online]. Available: http://www.ploughshares.org/issues-analysis/early-warning/iran-nuclear-compliance-implementation-day-here.html. [Accessed: 24-Jan-2016].

[9] "Building a Framework for Assurance, Accountability, and Action," *NTI Security Index: Theft, Sabotage*. [Online]. 3, pp. 4, 9. Available: http://www.ntiindex.org. [25-Jan. 2016].

[10] J. Fingas, 'Stuxnet worm entered Iran's nuclear facilities through hacked suppliers', 2014. [Online] Available: http:// http://www.engadget.com/2014/11/13/stuxnet-worm-targeted-companies-first/. [Accessed: 13-Mar-2016].

[11] Nrc.gov, 'Special Nuclear Material', 2015. [Online]. Available: http://www.nrc.gov/materials/sp-nucmaterials.html. [Accessed: 26-Jan-2016].

[12] Nrc.gov, 'Safeguard Categories of SNM', 2015. [Online]. Available: http://www.nrc.gov/security/domestic/mca/snm.html. [Accessed: 29 -Jan-2016].

[13] Iaea.org, 'Design Basis Threat (DBT)', 2014. [Online]. Available: http://www-ns.iaea.org/security/dbt.asp?s=4. [Accessed 30-Jan-2016].

[14] G. Aloise, “Nuclear Security: DOE and NRC have different security requirements for protecting weapons-grade material from terrorist attacks,” U.S. Government Accountability Office, Washington, D.C., Rep. 360882, Sept. 11, 2007. [Online]. Available: http://www.gao.gov/products/GAO-07-1197R

[15] D. J. Mitchell, “Neutron Detection with Gamma-Ray Spectrometers for Border Security Applications,” *IEEE Trans. Nucl. Sci.* vol. 57, pp. 2215-2219.

[16] Nrc.gov, 'Nuclear Security and Safeguards', 2015. [Online]. Available: http://www.nrc.gov/security.html. [Accessed: 2 -April-2016].

[17] R. C. Runkle, A. Bernstein, and P. E. Vanier. “Securing special nuclear material: Recent advances in neutron detection and their role in nonproliferation,” *Journal of Applied Physics,* vol. 108, pp. 0-0, Dec. 2010.

[18] L. Saldana, N. Stemen. 'Pulse Shape Discrimination Methods', Yale University, July 2014.

[19] J. Glodo, W.M. Higgins, E.V.D. van Loef, K.S. Shah, “Scintillation Properties of 1-inch Cs_2LiYCL_6:Ce Crystals,” *IEEE Trans. Nucl. Sci.*, 1206-1209 (2008).

[20] Bridgeport Instruments, LLC, 'e-Morpho MCA for Scintillator Detectors', 2013. [Online]. Available: http://www.bridgeportinstruments.com/products/emorpho/emorpho_brief_u11.pdf.

[21] S. Yousefi, L. Lucchese. “A wavelet-based pulse shape discrimination method for simultaneous beta and gamma spectroscopy,” *Nuclear Instruments and Methods in Physics Research A*, vol. 599, Nov. 2008.

[22] R. B. Walton, H. O. Menlove, 'Nondestructive Assay for Nuclear Safeguards', *Los Alamos Science*, No. 1, 1980.

[23] A. L. Nichols, D. L. Aldama, M. Verpelli. (2008, Aug.) *INDC International Nuclear Data Committee Handbook of Nuclear Data for Safeguards: Database Extensions,* Aug. 2008, International Atomic Energy Agency. Vienna, Austria. [Online]. Available: https://www-nds.iaea.org/sgnucdat/

[24] K. S. Krane. “Nuclear Fission” in *Introductory Nuclear Physics*. Hoboken, NJ: John Wiley & Sons, Inc., 1988, pp. 478-492.

[25] J. Lamarsh, A. Barratta. “Interaction of Radiation With Matter” in *Introduction to Nuclear Engineering*, 3rd Edition, Upper Saddle River, NJ: Prentice Hall, 2001, pp. 52-100.

[26] Nuclear Power, 'Neutron Energy', 2012. [Online]. Available: http://www.nuclear-power.net/nuclear-power/reactor-physics/atomic-nuclear-physics/fundamental-particles/neutron/neutron-energy/. [Accessed: 25-Mar-2016].

[27] K. S. Krane. "Detecting Nuclear Radiations" in *Introductory Nuclear Physics*. Hoboken, NJ: John Wiley & Sons, Inc., 1988, pp. 192-203.

[28] J. A. Coderre, class notes for Introduction to Ionization Radiation, Nuclear Science and Engineering, MIT, Fall, 2006.

[29] G. F. Knoll, *Radiation Detection and Measurement*, 3rd Edition, Ch. 16-17, John Wiley & Sons, 1999, pp. 585-680.

[30] T. W. Crane, M. P. Baker, "Neutron Detectors" in *Passive Nondestructive Assay of Nuclear Materials*, Los Alamos National Laboratory, pp. 379 – 406.

[31] A.P. Siddavatam, "Methods of Pulse Shape Discrimination (PSD)," *International Journal of Application or Innovation in Engineering & Management*, 1-7 (2014).

[32] B. D'Mellow, M.D. Aspinall, R.O. Mackin, M.J. Joyce, A.J. Peyton, "Digital discrimination of neutrons and γ-rays in liquid scintillators using pulse gradient analysis," *Science Direct*, May 2007.

[33] S. Flyckt, C. Marmonier. "Signal processing" in *Photomultiplier Tubes: Principles and Applications*. Brive, France: Photonis, 2002, pp. 42-44.

[34] R. Polikar, 'The Wavelet Tutorial', 1999. [Online]. Available: http://users.rowan.edu/~polikar/WAVELETS/WTtutorial.html. [Accessed: September – 2015].

[35] U. Lepik, H. Hein, *Haar Wavelets With Applications*. Gewerbestrasse, Switzerland: Springer International, 2014, pp. 7 – 20.

[36] J. R. Taylor, *An Introduction to Error Analysis: The Study of Uncertainties in Physical Measurements*, 2nd Edition, Sausalito, CA: University Science Books, 1997, pp. 121-149.

[37] G. Ranucci, "An analytical approach to the evaluation of the pulse shape discrimination properties of scintillators," *Nuclear Instruments & Methods Research Section A*, vol. 354, pp. 389-399, June 1994.

[38] Winyard, R.A., Lutkin, J.E., and McBeth, G.W., "Pulse shape discrimination in inorganic and organic scintillators," *Nuclear Instruments and Methods*, vol. 95, pp. 141-153, 1971.

[39] J. Prekeges. "Scintillation Detectors" in *Nuclear Medicine Instrumentation*, 2nd Edition, Burlington, MA: Jones & Bartlett Learning, 2013, pp. 17-27.

[40] The Radiation Information Network, 'Measurement of Radiation, Sodium Iodide Detector', 2011. [Online]. Available: http://www.physics.isu.edu/radinf/naidetector.htm. [Accessed: 20-Mar-2016].

[41] K. S. Krane. “Nuclear Decay and Radioactivity” in *Introductory Nuclear Physics*. Hoboken, NJ: John Wiley & Sons, Inc., 1988, pp. 207-213.

[42] J. Glodo, R. Hawrami, E. van Loef, U. Shirwadkar, K. Shah, “Pulse Shape Discrimination With Selected Elpasolite Crystals,” *IEEE Trans. Nucl. Sci.*, vol. 59, pp. 2328-2333, Oct. 2012.

[43] Scintillation Detectors, 'Scintillator Response To γ-rays', [Online]. Available: http://scionix.nl/scintillator.htm#energyres. [Accessed: 5-April-2016].

[44] N. Khan, R. Machrafi, “Neutron and Gamma-ray Detection using a Cs_2LiYCl_6 Scintillator,” *EPJ Web of Conferences*, vol. 66, pp. 11018-p.1 – 11018-p.4, 2014.

[45] *Photomultiplier Tubes: Basics and Applications*, 3rd ed., Hamamatsu Photonics K. K., Hamamatsu, Japan, 2007, pp. 2.

[46] Hamamatsu.com, 'Photomultiplier tube R6231-100', 2016. [Online]. Available: https://www.hamamatsu.com/us/en/R6231-100.html. [Accessed: 12-April-2016].

[47] Microanalyst.net, 'The Energy Dispersive System (X-Ray Spectrometer) EDS/EDX', 2016. [Online]. Available: http://microanalyst.mikroanalytik.de/index_e.phtml. [Accessed: 27-Mar-2016].

[48] eMorpho User’s Manual Data Sheet, Version R1, Bridgeport Instruments, LLC, Austin, TX, 2009, pp. 7 - 12.

[49] A. Akansu, W. Serdijn, I. Selesnick, “Emerging applications of wavelets: A review,” *Physical Communication*, vol. 3, pp. 1-18, 2010.

CURRICULUM VITAE

Brittany Morgan

E-mail: morga214@unlv.nevada.edu
LinkedIn: http://linkedin.com/in/brittany-morgan-a9881255

EDUCATION

Aug. 2014 – May 2016 (expected)	University of Nevada Las Vegas *M.S. Materials and Nuclear Engineering* *Graduate Certificate in Nuclear Safeguards and Security*
Mar. 2009 – June 2011	Seattle University *B.A. Physics*

AWARDS

Aug. 2015 – May 2016	National Security Technologies Scholarship: $6000

PRESENTATIONS

July 2016	INMM 57th Annual Meeting **Will be presenting on neutron-gamma discrimination in elpasolite scintillator detector*
Apr. 2016	UNLV College of Engineering Graduate Celebration *3rd Place in Poster Competition, awarded $250*
Apr. 2015	ANS Student Conference *Presented computational study of whole-body X-ray imaging system*